Design and Analysis of a Dual-Mode Flux-Switching Doubly Salient DC-Field Magnetless Machine for Wind Power Harvesting

Christopher H. T. Lee, K. T. Chau, and Chunhua Liu

Department of Electrical and Electronic Engineering, The University of Hong Kong, Hong Kong, China

This paper proposes a new dual-mode flux-switching doubly salient DC-field (FS-DSDC) machine for the wind power harvesting applications. The key distinction of the proposed machine is to artfully incorporate the design concepts of two machines, namely the FSDC and the DSDC machines together. By regulating the winding configurations, the proposed machine can behave similarly as the corresponding machines do and hence achieving the dual-mode operations, namely the FSDC mode and DSDC mode, to offer higher flexibility and stability for different wind situations. The proposed machine can utilize its external DC-field winding to tune its flux density effectively, hence providing the constant-voltage charging function at various wind speeds and loads. The corresponding performances of the proposed machine are analyzed by using the finite element method (FEM) and verified by experimental results.

***Index Terms*—Magnetless machine, dual-mode, flux-switching, doubly salient, wind power harvesting.**

I. INTRODUCTION

BECAUSE of the growing attentions on the issues about the energy crisis and the environmental pollution, as one of the most promising as well as cost-comparative solutions, the wind power harvesting has become a hot research topic recently [1–3]. In general, the wind power harvesting applications can be categorized into two major types, namely the constant-speed constant-frequency (CSCF) wind power generation and the variable-speed constant-frequency (VSCF) wind power generation [4]. Without adopting any power converters, the CSCF type enjoys the definite advantages of simple system structure and also high robustness [5]. However, its turbine speed is always kept constant and has no connection with the variation of the wind speed. Hence, it suffers from the low efficiency and high mechanical stress problems.

Upon the development of the power electronics, the VSCF system can be adopted effectively. The VSCF system is able to capture the maximum wind power with a variable turbine speed along with the wind speed [6, 7]. Not surprisingly, the VSCF type can offer higher efficiency than the CSCF does. As the soul of the VSCF system, the electric machines have to fulfill several criteria, including satisfactory efficiency level, high power density, easy to control, wide-speed operating range, limited-maintenance, and fault-tolerant capability [8–10]. The doubly salient permanent-magnet (DSPM) machines, which can achieve these goals, have been actively developed [11, 12]. However, the DSPM machines suffer from the problems of high PM material

cost and also the uncontrollable PM flux [13, 14]. To cope with these profound problems, the magnetless machines, namely the switched reluctance (SR) and the doubly salient DC-field (DSDC) machines have gained more attentions recently [15, 16]. Based on the controllable DC-field winding, the DSDC can regulate its flux density effectively and hence is suitable for the low-torque high-speed situation [17]. Meanwhile, the flux-switching DC-field (FSDC) machine that offers the bipolar flux-linkage is favorable for high-torque low-speed situation [18]. Even though the generator speed in the wind power generation is limited in a specific range, where each of the mentioned machines may fulfill all its needs accordingly, the development of the new machine with higher flexibility and stability is always desirable.

This paper aims to artfully combine the design equations of the FSDC and DSDC machines together, to form a new dual-mode FS-DSDC machine, purposely for the wind power harvesting applications. By adopting different winding configurations, the proposed machine behaves similarly as the corresponding machines do. Hence, it can operate with two different operating modes, namely the FSDC mode for low-speed situation and the DSDC mode for high-speed situation. The finite element method (FEM) is employed to analyze the machine performances, and the experimental prototype is also build for verifications.

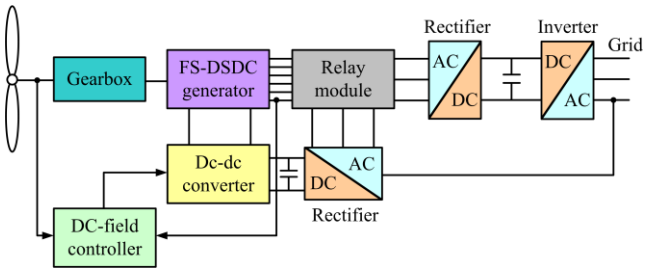

Fig. 1. Proposed wind power generation system.

II. System Configuration and Speed Consideration

Fig. 1 shows the proposed configuration of the wide-speed range wind power generation which consists of the following key elements: (i) a wind turbine with gearbox to capture the wind power, (ii) the proposed FS-DSDC machine to perform the electromechanical energy conversion, (iii) the power electronic relay module to switch the winding configurations, (iv) two 3-phase full-bridge rectifiers to perform the ac-dc conversion for two different operation modes, (v) two batteries to store the captured energy, (vi) a buck converters based on the DC-field controller signal to regulate the rectified dc voltage, and (vii) an inverter to perform the dc-ac conversion connecting to the power grid.

According to the Betz's theory, the mechanical power captured by the wind turbine can be described as [4]:

$$P_{mech} = \frac{1}{2} C_p \rho v_\omega^3 A \qquad (1)$$

where C_p is the coefficient of wind power conversion factor with a typical value of 0.4 or below, ρ is the air density, v_ω is the wind velocity, and A is the swept area of the wind-turbine rotor. The value of C_p is a function based on the ratio of the blade tip speed to the wind speed β, and defined as:

$$\beta = \frac{\omega R}{v_\omega} \tag{2}$$

where R is the radius of the blades and ω is the rotational speed of the wind-turbine shaft. For a specific value β_{max}, the power conversion factor C_p can reach to a single maximum in order to capture the maximum mechanical power from the wind speed. As expected, the shaft speed should align with the wind speed to maximize its total power output. When the turbine runs at the β_{max}, the maximum output power can then be described as:

$$P_{mech} = \frac{1}{2}(C_{p\max}\pi R^2 \rho)v_\omega^3 \tag{3}$$

According to equation (2) and (3), the maximum output power can be further deduced as:

$$P_{mech} = \frac{1}{2}(\frac{C_{p\max}\pi R^5 \rho}{\beta_{\max}^3})\omega^3 \tag{4}$$

It should be noted that the rotor speed of the wind generator is typical below 1000 rpm at the normal situation, while is higher than 1000 rpm at the strong wind situation [4].

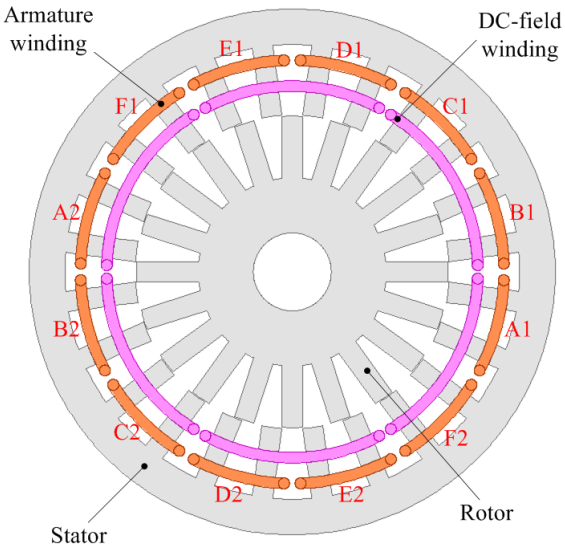

(a)

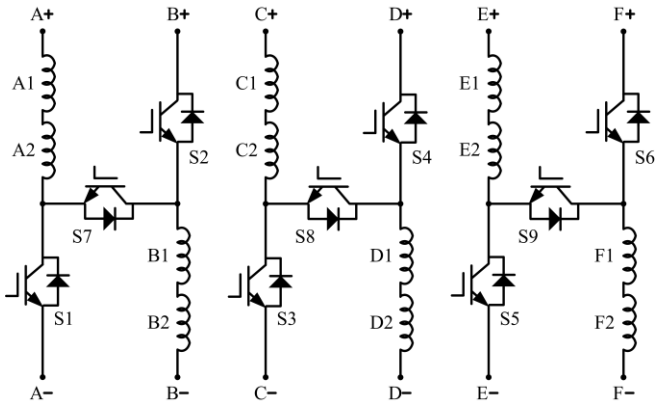

(b)

Fig. 2. Proposed dual-mode FS-DSDC machine: (a) Proposed machine structure. (b) Proposed winding connection configurations.

III. Proposed Dual-Mode FS-DSDC Machine

A. Proposed Machine Topology

The topology of the proposed dual-mode FS-DSDC machine that employs into the proposed wind power system is shown in Fig. 2(a). The proposed FS-DSDC machine purposely combines the design philosophies of both FSDC and DSDC machines together, hence allowing itself to operate with two different operating modes, namely the FSDC mode and the DSDC mode. The design criteria for the FSDC and the DSDC machines are based on the equations (1) and (2), as shown respectively [17, 18]:

$$\begin{cases} N_{sp} = 2mi \\ N_{se} = N_{sp} N_{st} \quad (N_{st} = 2,4\ldots) \\ N_r = N_{se} - N_{sp} \pm 2i \end{cases} \tag{5}$$

$$\begin{cases} N'_{sp} = 2m' j \\ N'_{se} = N'_{sp} N'_{st} \\ N'_r = N'_{se} \pm 2k \end{cases} \tag{6}$$

where m, N_{sp}, N_{st}, N_{se}, and N_r are the number of armature phases, the stator pole, the stator teeth, the equivalent stator pole and the rotor pole for FSDC, respectively; m', N'_{sp}, N'_{st}, N'_{se}, and N'_r are the armature phases, the stator pole, the stator teeth, the equivalent stator pole and the rotor pole for DSDC, respectively; i, k and j are any integers. To incorporate the design equations between the two machines, the number of equivalent stator poles of the two machines, ie: N_{se} and N'_{se} are purposely equalized and the following equality can be deduced:

$$(mi)N_{st} = (m' j)N'_{st} \tag{7}$$

However, the result ends up with infinite many solutions and in order to reduce the degree of freedom, i and j are specifically equalized and the following relationship is derived:

$$\frac{N_{st}}{N'_{st}} = \frac{m'}{m} \quad (m \neq m') \tag{8}$$

Similarly, the number of the rotor pole of the two machines, ie: N_r and N'_r are equalized and by equation (8), the following equality can be further deduced:

$$k = (m-1)i \tag{9}$$

Based on the equations (5), (6), (8) and (9), the fundamental design combinations of the proposed machine are formed and categorized in Table I. To simplify the control complexity, the 3-phase and 6-phase topologies, ie: m = 3 and m' = 6 are chosen. Meanwhile, to favor the relative low-speed operating range, from 0 – 1000 rpm at normal wind situation, the multi-tooth

structure, ie: N_{st} = 4 and N'_{st} = 2 is more preferable compared with its single-tooth counterpart, ie: N_{st} = 2 and N'_{st} = 1 [14]. By considering these concerns, the following combinations are chosen: N_{se} = 24, and N_r = 20, as the proposed structure for the FS-DSDC machine.

Compared with the traditional generators, the proposed one consists of the independent field excitation, which extends its flexibility to cope with different operating situations. Even though the voltage regulation can be performed by the back-to-back converters, the proposed generator can utilize its inherited flux regulating ability to act as the all-in-one system to perform all tasks as a whole. In addition, the proposed generator can be operated with two operating modes, or technically regarded as with different operating phases. Hence, the proposed generator can offer higher degree of fault-tolerability, as compared with its counterparts [3].

TABLE I. FUNDAMENTAL DESIGN COBMINATIONS
OF THE PROPOSED FS-DSDC MACHINE

m	***m'***	***i***	***j***	***k***	N_{st}	N'_{st}	$N_{se}=N'_{se}$	$N_r=N'_r$
3	6	1	1	2	2	1	12	8
3	6	1	1	2	4	2	24	20
4	8	1	1	3	2	1	16	10

B. Dual-Mode Operating Principle

Both of the two winding sets adopt the concentrated winding arrangements, which can be constructed easily. Each of the armature winding loop is purposely separated conducted and all of them can then be independently controlled. Therefore, different connection configurations can be achieved upon the help of the power electronic relay module.

The proposed armature winding connections at different modes, namely the FSDC and DSDC mode are shown in Fig. 2(b). At the FSDC mode, the switches S1, S2, S3, S4, S5, and S6 are off, while S7, S8, and S9 are on, such that the armature windings are connected as A1, A2, B1, B2, C1, C2, D1, D2, E1, E2, F1, and F2, behaving similarly as a 3-phase FSDC machine does. Meanwhile, at the DSDC mode, the switches S1, S2, S3, S4, S5, and S6 are on, while S7, S8, and S9 are off, such that the armature windings are connected in a way similarly as a 6-phase DSDC machine does.

The winding configuration of the proposed machine at the FSDC mode behaves similarly as the two corresponding armature windings connecting in series, such that the generated voltage is larger than that from the DSDC mode has. Since the generated voltage varies along with the wind speed accordingly, the FSDC mode should be employed for the low-speed environment, such that the generated voltage won't exceed the charging limit. Meanwhile, the DSDC mode should be employed for the high-speed environment instead.

Through the relay module, the 3-phase armature winding at FSDC mode can be switched to connect with one single 3-phase full-bridge rectifier to perform the ac-dc conversion to charge up the battery and then transfer the energy to the grid via the

inverter. On the other hand, the 6-phase armature winding at DSDC mode can then be switched to connect with two 3-phase full-bridge rectifiers, in which one of them to transfer energy to the grid and one to charge up the battery as the energy storage for the DC-field excitation. This arrangement can ensure that the generated DC voltage will never exceed the threshold voltage limit, even at the extreme high wind speed environment. In addition, the independent DC-field energy storage can eliminate the reliance on the grid, leading to minimize the interference to the power grid.

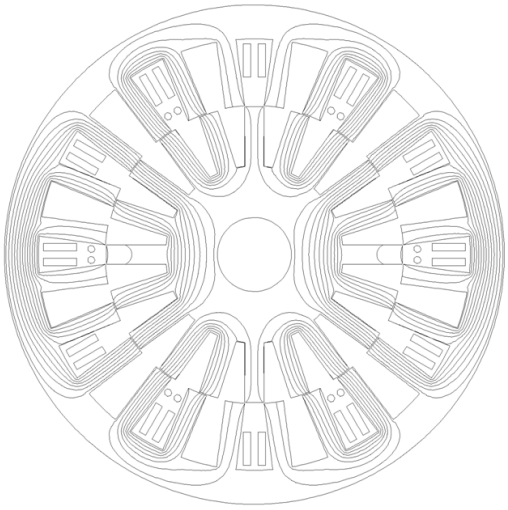

Fig. 3. Magnetic field distribution of the proposed FS-DSDC machine.

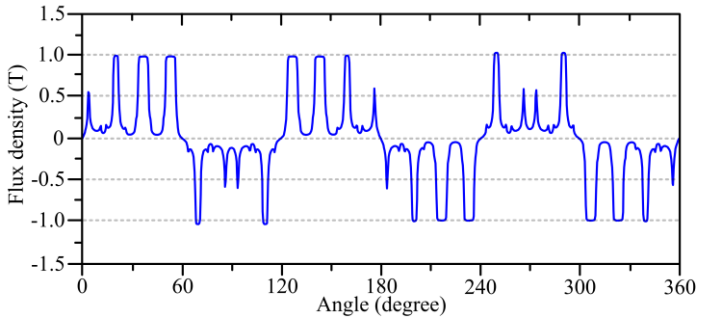

Fig. 4. Airgap flux density of the proposed FS-DSDC machine.

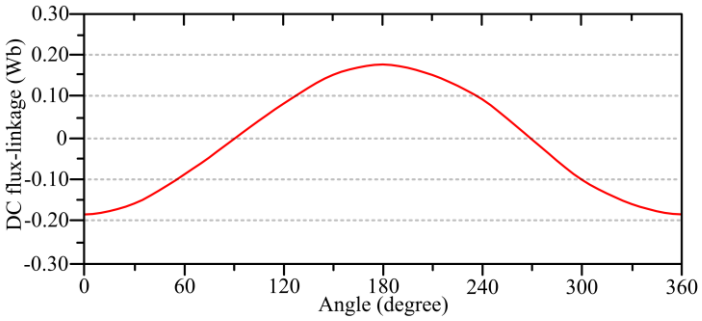

(a)

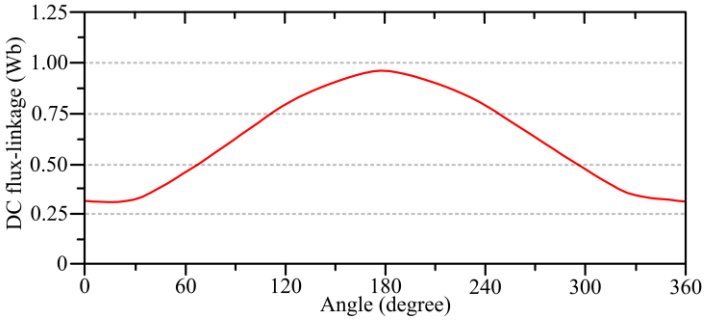

(b)

Fig. 5. DC flux-linkage waveforms: (a) FSDC mode. (b) DSDC mode.

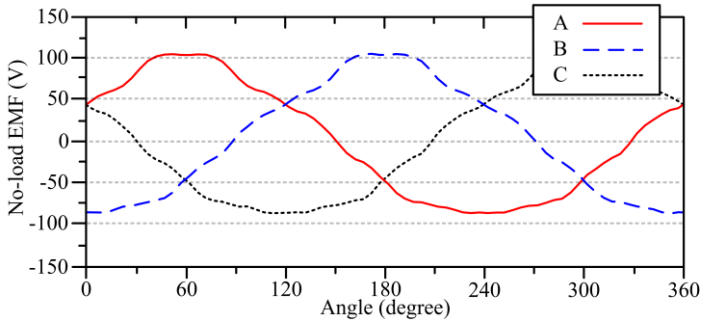

(a)

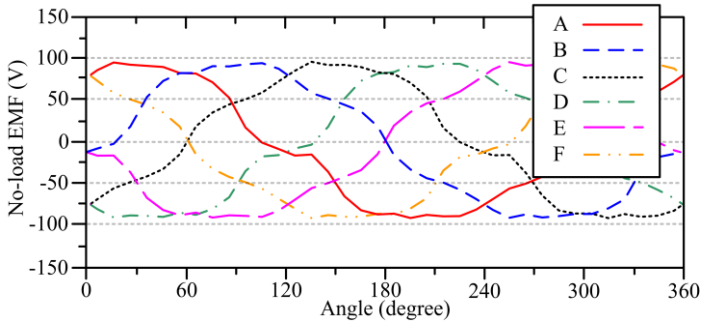

(b)

Fig. 6. No-load EMF waveforms: (a) At FSDC mode with speed of 300 rpm. (b) At DSDC mode with speed of 600 rpm.

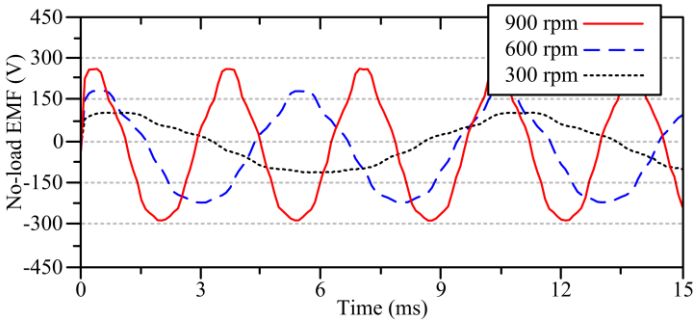

(a)

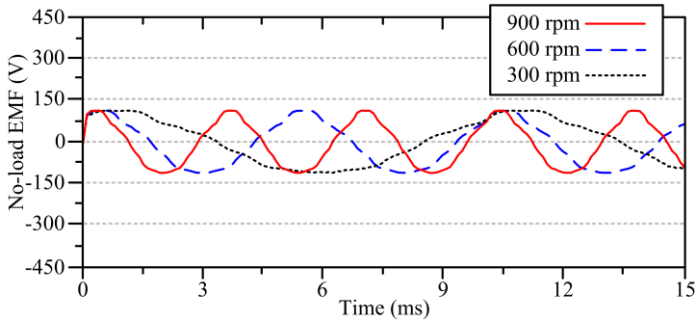

(b)

Fig. 7. No-load EMF waveforms at FSDC mode with various operating speeds: (a) Without flux regulation. (b) With flux regulation.

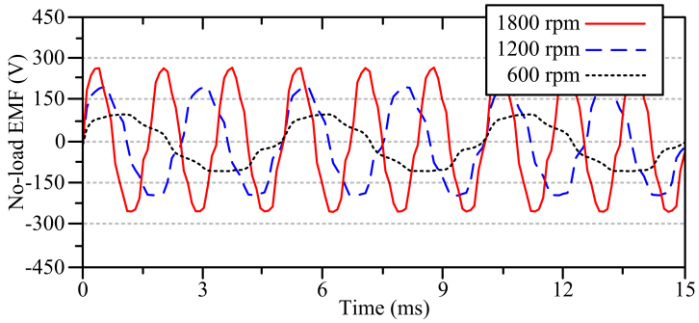

(a)

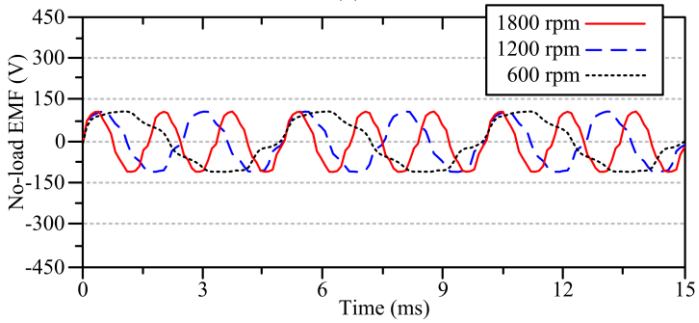

(b)

Fig. 8. No-load EMF waveforms at DSDC mode with various operating speeds: (a) Without flux regulation. (b) With flux regulation.

IV. Finite Element Method Analysis

In many years, the electromagnetic field analysis has always been one of the most accurate and convenient tools to perform the electric machine analysis. Basically, it can be categorized into two major subsidiaries, namely the analytical field calculation [19] and the numerical field calculation [20]. To model the machine performances, the electromagnetic field equation is described as [4]:

$$\begin{cases} \Omega: \dfrac{\partial}{\partial x}\left(v\dfrac{\partial A}{\partial x}\right)+\dfrac{\partial}{\partial y}\left(v\dfrac{\partial A}{\partial y}\right)=-(J_z+J_f) \\ A\big|_S=0 \end{cases} \tag{10}$$

where Ω is the field solution region, A *and* J_z the z-direction components of vector potential and current density, respectively, J_f the equivalent current density of the excitation field, S the Dirichlet boundary, and v the reluctivity. In addition, the equivalent circuit equation during generation is governed by:

$$(R+R_L)i_s+(L+L_L)\frac{di}{dt}-\frac{l}{s}\iint_{\Omega}\frac{\partial A}{\partial t}d\Omega=0 \tag{11}$$

where R is the winding resistance, R_L the load resistance, L the end winding inductance, L_L the load inductance, l the axial length, and s the conductor area of each turn of phase winding. The FEM is applied to analyze the machine performances of the proposed FS-DSDC machine and the JMAG-Designer is employed as the magnetic solver to perform the FEM. The magnetic field distribution of the proposed machine at no-load condition is shown in Fig. 3.

The airgap flux density waveform of the proposed machine at no-load condition is shown in Fig. 4. The results show the original flux of each stator pole is modulated into four portions in accordance with the number of teeth per stator pole. According to the corresponding winding configurations, the proposed machine at FSDC mode acts similarly as the 4-toothed FSDC machine does, while at DSDC mode as the 2-toothed DSDC machine does.

The DC flux-linkage waveforms at the FSDC mode and at the DSDC mode are shown in Fig. 5(a) and Fig. 5(b), respectively. The simulation waveforms show that the proposed machine obtains the bipolar DC flux-linkage pattern at FSDC mode, while the unipolar DC flux-linkage pattern at DSDC mode. These results confirm that the pole-pair arrangements and the armature winding configurations of the proposed machine are correct, hence, further verifying the proposed design equations are also correct.

By performing FEM, the performances of the proposed wind power generation system can be analyzed thoroughly. The no-load electromagnetic force (EMF) waveforms of the FS-DSDC machine at FSDC mode under the operating speed of 300 rpm and at DSDC mode of 600 rpm are shown in Fig. 6(a) and Fig. 6(b), respectively. It can be shown that the no-load EMF waveforms at FSDC mode are well balanced among 3-phase pattern without significant distortion, while at DSDC mode are 6-phase waveforms with symmetrical pattern instead. The magnitudes of the no-load EMF among each phase at FSDC mode is approximately the same compared with those at DSDC mode are. Hence, these confirm that the FSDC mode should be adopted at the low-speed environment, while the DSDC mode at the high-speed environment.

In addition, the no-load EMF waveforms under the FDSC mode and DSDC mode at various speeds under two conditions, namely without and with flux regulations are shown in Fig. 7 and Fig. 8, respectively. Undoubtedly, without any DC-field flux regulations, both the generated voltages at two modes vary along with the varying speeds. Therefore, the output voltages may overcharge the battery and harm the whole wind power system. Meanwhile, the DC-field level can be tuned purposely in order to keep the output voltages as constant as possible over the wide-speed ranges.

TABLE II. KEY DATA OF PROPOSED MACHINE

Items	**FS-DSDC**
Stator outside diameter	270.0 mm
Stator inside diameter	161.2 mm
Rotor outside diameter	160.0 mm
Rotor inside diameter	40.0 mm
No. of equivalent stator poles	24
No. of rotor poles	20
Stator pole arc	7.5°
Rotor pole arc	7.5°
Stator pole height	36 mm
Rotor pole height	32 mm
Airgap length	0.6 mm
Stack length	80.0 mm
No. of turns per armature coil	100

V. EXPERIMENTAL VERIFICATION

For verification, the experimental setup of the proposed wind power generator under the open-loop mode is established and as shown in Fig. 9. The corresponding key design data of the proposed FS-DSDC machine is listed in Table II.

The measured no-load EMF waveforms of the proposed FS-DSDC machine at FSDC mode and DSDC mode under the corresponding conditions are shown in Fig. 10. As shown, the measured waveforms are slightly different from the simulated ones as shown in Fig. 6(a) and Fig. 6(b), and the differences are generally caused by the manufacturing imperfection. Meanwhile, the experimental results are still within the normal range and the discrepancies are expected to be acceptable. In addition, the measured no-load EMF waveforms at FSDC mode under the higher speed of 900 rpm and at DSDC mode of 1800 rpm, without and with the DC-field flux regulations are shown in Fig. 11. Since all the no-load EMF waveforms of the 6-phase windings at DSDC mode are well balanced and symmetrical, to have a better illustration, only the phase-A, -C, and -E are shown purposely. With the flux regulation, the magnitudes of the no-load EMF waveforms at higher speed ranges can be kept at the same level as compared with those at the lower speed ranges. These measured waveforms verify the expected performances by the simulation waveforms in Fig. 7 and Fig. 8, and confirm the proposed wind power generation system is able to maintain the generated voltages to become as constant as possible over a wide range of operating speeds, even under the strong wind situation.

Through the 3-phase rectifications, the simulated and the measured DC charging voltages at the FSDC and at DSDC modes are shown in Fig. 12. The single output at FSDC mode can be connected to the grid for energy transferring, while the two outputs at DSDC mode can be connected to the grid and also to the DC-field energy storage device. In addition, the corresponding simulated and measured DC charging voltage characteristics at FSDC mode and at DSDC mode, without and with the flux regulations, with respect to the operating speed at no-load are shown in Fig. 13, and the measured results well agree with the simulated ones. The results verify that the proposed wind power generation system can utilize the flux regulating ability to

maintain the DC charging voltages at the certain level, hence protecting the whole system. Meanwhile, the charging performances of the proposed system under the load conditions are also studied. The corresponding simulated and measured DC charging voltage characteristics at FSDC mode under the operating speed of 900 rpm and at DSDC mode of 1800 rpm, without and with the flux regulations, with respect to the load current are shown in Fig. 14. Once again, by regulating the DC-field winding, the DC charging voltages can be kept at the specific level. Therefore, the results further verify the proposed wind power generation system can perform as a constant-voltage generator at the wide range of wind speeds and load currents. Finally, the efficiencies of the proposed machine at two modes as the function of speeds have been measured and shown in Fig. 15. It can be found that the proposed machine at both modes can achieve comparable efficiencies as compared with the profound machines do, where the efficiency of the magnetless SR generator is around 70 % [16]. Particularly, the efficiencies of the proposed machine at FRDC mode and at DSDC mode can achieve approximately 74 % and 72 %, respectively.

Fig. 9. Experimental setup of the proposed wind power generation system.

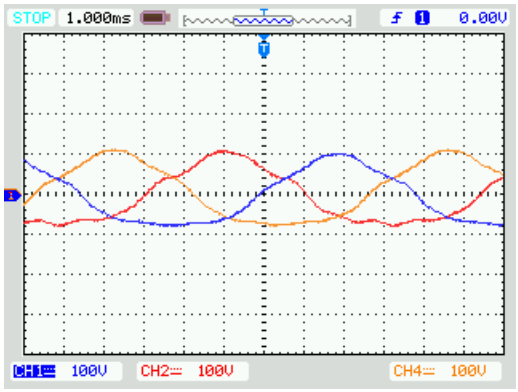

(a)

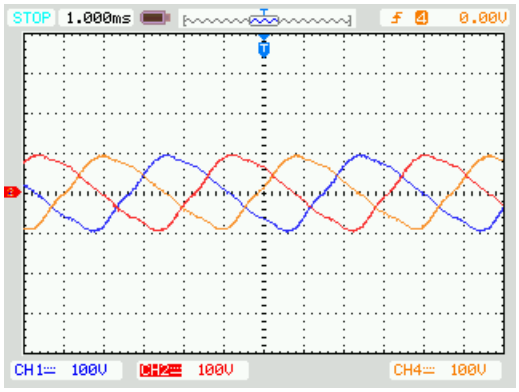

(b)

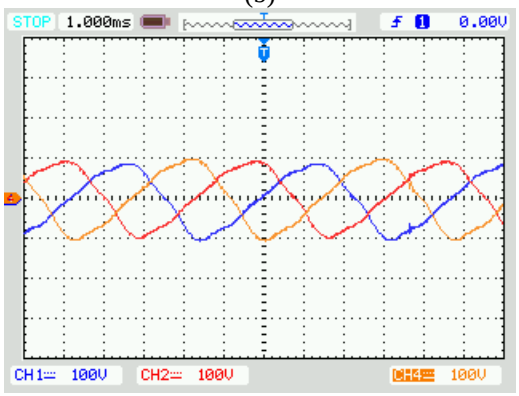

(c)

Fig. 10. Measured no-load EMF waveforms: (a) FSDC mode. (b) Phase-A, -C, and -E under DSDC mode. (c) Phase-B, -D, and -F under DSDC mode.

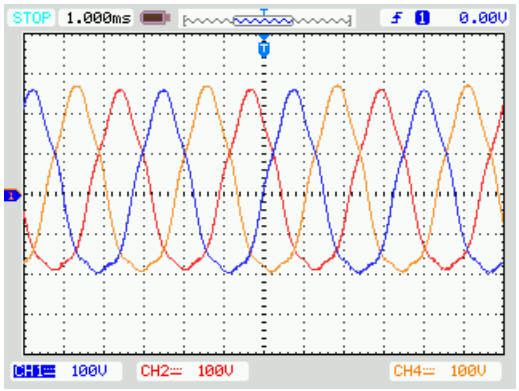

(a)

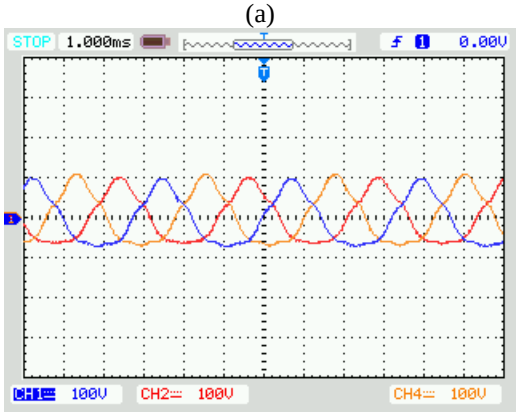

(b)

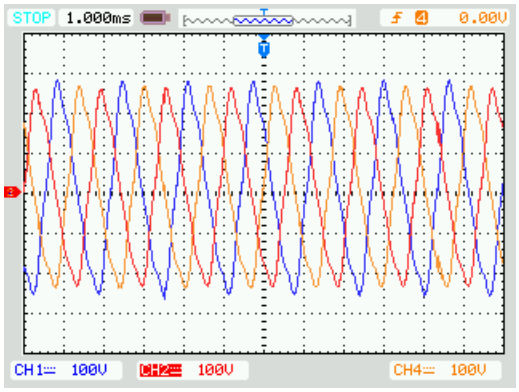

(c)

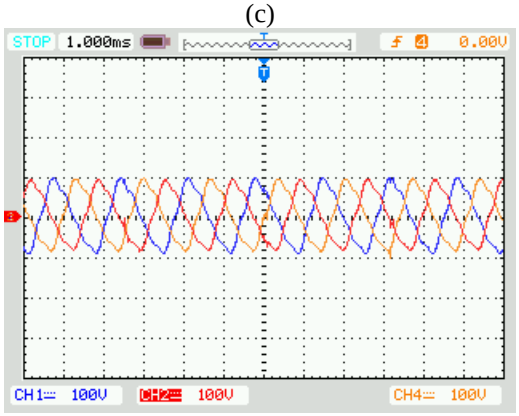

(d)

Fig. 11. Measured no-load EMF waveforms: (a) Without flux regulation of FSDC mode at 900 rpm. (b) With flux regulation of FSDC mode at 900 rpm. (c) Without flux regulation of DSDC mode (Phase-A, -C, and -E) at 1800 rpm. (d) With flux regulation of DSDC mode (Phase-A, -C, and -E) at 1800 rpm.

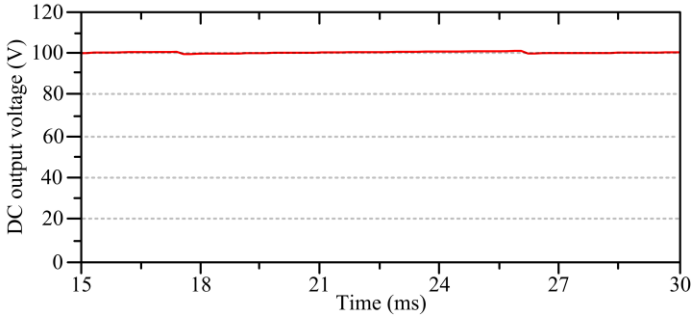

(a)

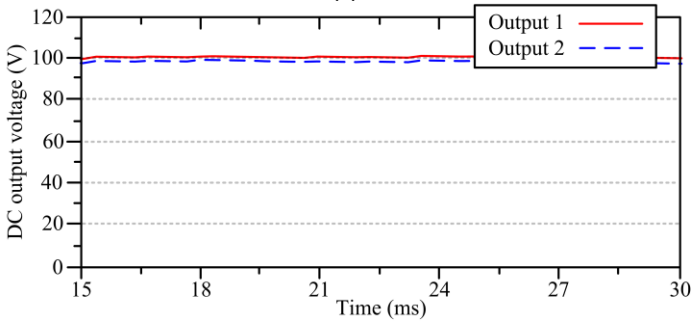

(b)

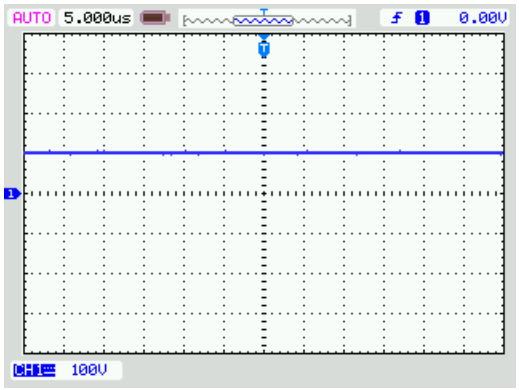

(c)

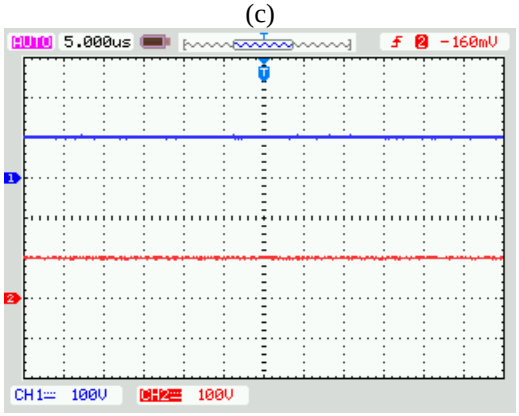

(d)

Fig. 12. DC charging voltages: (a) Simulated result of FSDC mode. (b) Simulated result of DSDC mode. (c) Measured result of FSDC mode. (d) Measured result of DSDC mode.

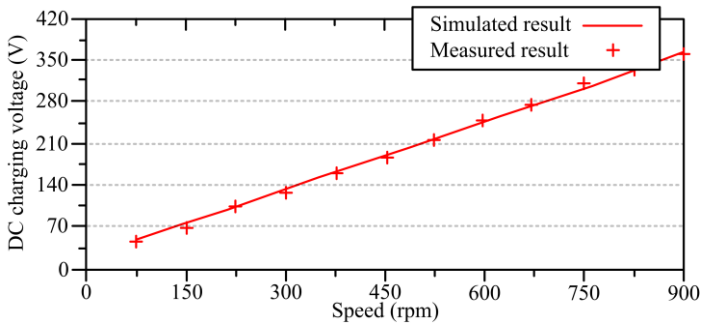

(a)

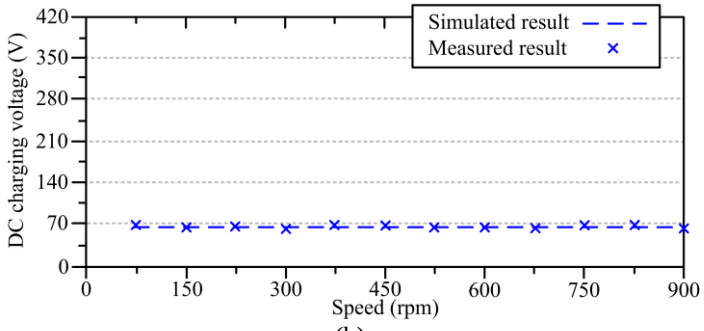

(b)

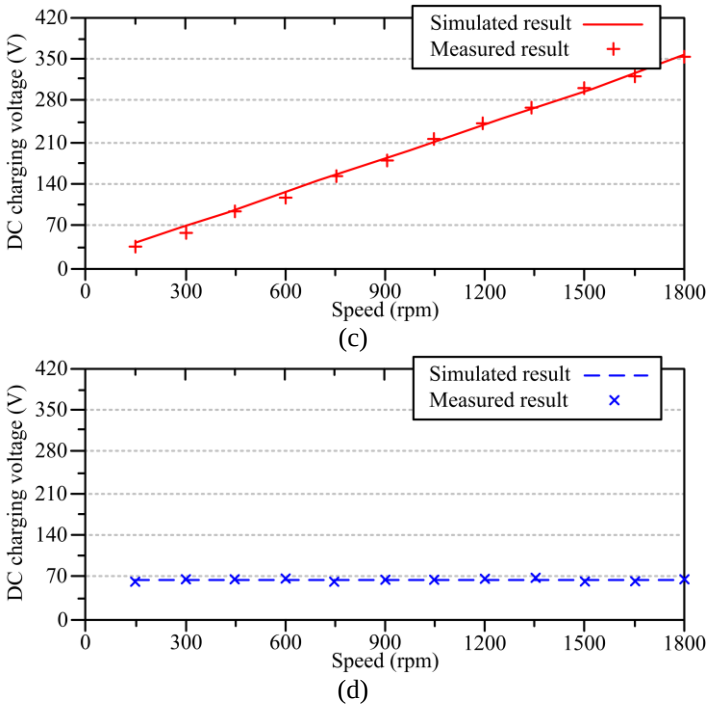

Fig. 13. Charging voltage characteristics versus speed at no load: (a) FSDC mode – without flux regulations. (b) FSDC mode – with flux regulations (c) DSDC mode – without flux regulations. (d) DSDC mode – with flux regulations.

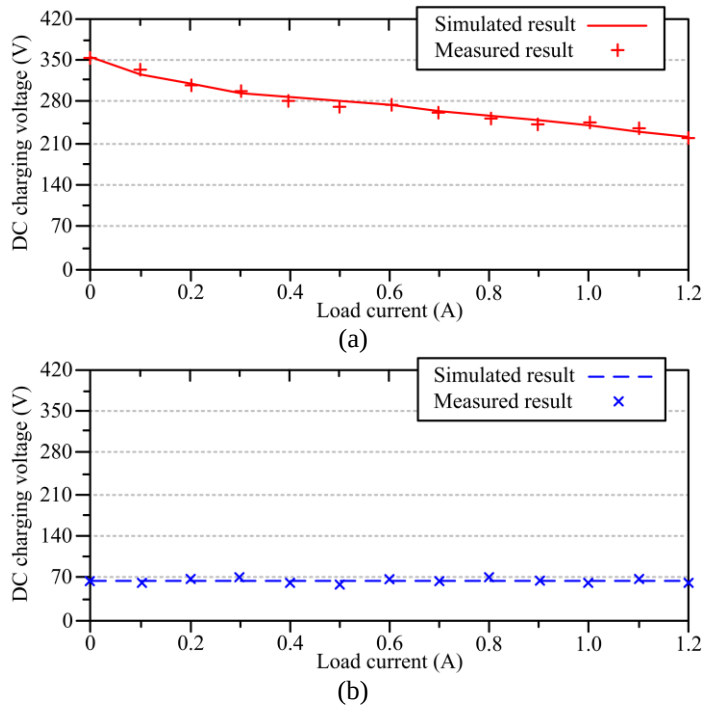

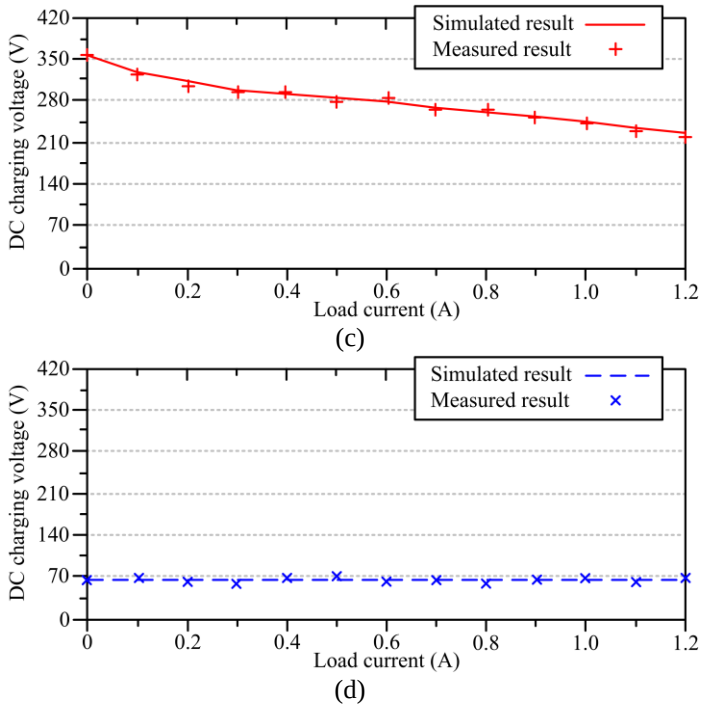

Fig. 14. Charging voltage characteristics versus load current: (a) FSDC mode – without flux regulations. (b) FSDC mode – with flux regulations (c) DSDC mode – without flux regulations. (d) DSDC mode – with flux regulations.

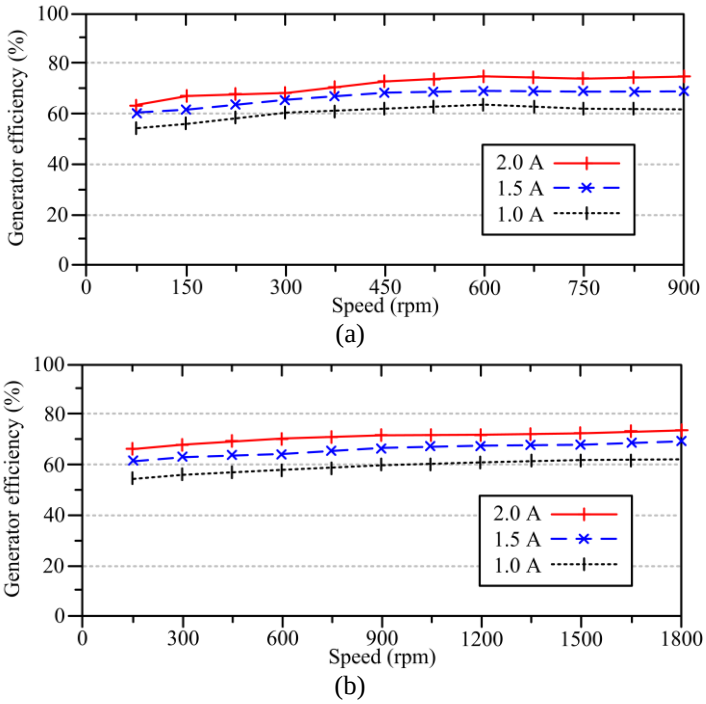

Fig. 15. Measured efficiencies versus speed at different loads: (a) FSDC mode. (b) DSDC mode.

VI. CONCLUSION

This paper introduces a new dual-mode FS-DSDC machine for wind power harvesting applications. The key of the proposed machine is to purposely incorporate two machine design philosophies together, hence allowing the machine to offer higher

flexibility and stability to cater different possible situations. Based on the independent DC-field excitations, the proposed machine can produce the controllable airgap flux densities, hence accomplishing the constant-voltage charging characteristics over a wide-speed range under different load currents. Without implementation of any PM material, the proposed magnetless machine takes the absolute advantage of cost-benefit compared with its PM counterparts. Both the FEM simulations and experimental results confirm the validity of the proposed wind power harvesting system.

VII. Acknowledgment

This work was supported by a grant (Project No. 17200614) from Hong Kong Research Grants Council, Hong Kong Special Administrative Region, China.

References

[1] Ault, G.W., Bell, K.R.W., Galloway, S.J.: 'Calculation of economic transmission connection capacity for wind power generation', *IET Renew. Power Gener.*, 2007, **1**, (1), pp. 61–69

[2] Luickx, P.J., Delarue, E.D, D'haeseleer, W.D.: 'Effect of the generation mix on wind power introduction', *IET Renew. Power Gener.*, 2008, **3**, (3), pp. 267–278

[3] Chau, K.T., Li, W., Lee, C.H.T.: 'Challenges and opportunities of electric machines for renewable energy', *Prog. Electromagn. Res. B*, 2012, **42**, pp. 45–74

[4] Jian, L., Chau, K.T., Jiang, J.Z.: 'A magnetic-geared outer-rotor permanent-magnet brushless machine for wind power generation', *IEEE Trans. Ind. Appl.*, 2009, **45**, (3), pp. 954–962

[5] Grauers, A.: 'Efficiency of three wind energy generator systems', *IEEE Trans. Energy Convers.*, 1996, **11**, (3), pp. 650–657

[6] Kanellos, F.D., Hatziargyriou, N.D.: 'Control of variable speed wind turbines equipped with synchronous or doubly fed induction generators supplying islanded power systems', *IET Renew. Power Gener.*, 2009, **3**, (1), pp. 96–108

[7] Lin, H., Liu, X., Zhu, Z.Q., Fang, S.: 'Analysis and control of a dual-stator hybrid excitation synchronous wind generator', *IET Electr. Power Appl.*, 2011, **5**, (8), pp. 628–635

[8] Campos-Delgado, D.U., Espinoza-Trejo, D.R., Palacios, E.: 'Fault-tolerant control in variable speed drives: a survey', *IET Electr. Power Appl.*, 2008, **2**, (2), pp. 121–134

[9] Cheng, M., Hua, W., Zhang, J., Zhao, W.: 'Overview of stator-permanent magnet brushless machines', *IEEE Trans. Ind. Electron.*, 2011, **58**, (11), pp. 5087–5101

[10] Keysan, O., Mueller, M.A.,: 'Superconducting generators for renewable energy applications', *Proc. IET Conf. Renew. Power Gener.*, Edinburgh, Sept. 2011, pp. 1–6

[11] Chau, K.T., Chan, C.C., Liu, C.: 'Overview of permanent-magnet brushless drives for electric and hybrid electric vehicles', *IEEE Trans. Ind. Electron*., 2008, **55**, (6), pp. 2246–2257

[12] Zhang, J., Cheng, M., Chen, Z., Hua, W.: 'Comparison of stator-mounted permanent-magnet machines based on a general power equations', *IEEE Trans. Energy Convers*., 2009, **24**, (4), pp. 826–834

[13] Pang, Y., Zhu, Z.Q., Howe, D.: 'Analytical determination of optimal split ratio for permanent magnet brushless motor', *IEE Electr. Power Appl*., 2006, **153**, (1), pp. 7–13

[14] Wang, Y., Cheng, M., Chen, M., Du, Y., Chau, K.T.: 'Design of high-torque-density double-stator permanent magnet brushless motors', *IET Electr. Power Appl*., 2011, **5**, (3), pp. 317–323

[15] Chau, K.T., Cheng, M., Chan, C.C.: 'Nonlinear magnetic circuit analysis of a novel stator-doubly-fed doubly-salient machine', *IEEE Trans. Magn.*, 2002, **38**, (5), pp. 2282–2384

[16] Lee, C., Krishnan, R., Lobo, N.S.: 'Novel two-phase switched reluctance machine using common-pole E-core structure: concept, analysis, and experimental verification', *IEEE Trans. Ind. Appl*., 2009, **45**, (2), pp. 703–711

[17] Lee, C.H.T., Liu, C., Chau, K.T.: 'A magnetless axial-flux machine for range-extended electric vehicles', *Energies*, 2014, **7**, (3), pp. 1483–1499

[18] Lee, C.H.T., Chau, K.T., Liu, C.: 'Design and analysis of a new multitoothed magnetless doubly-salient machine', *IEEE Trans. Appl. Supercond.*, 2014, **24**, (3), p. 5200804

[19] Zheng, P., Zhao, Q., Bai, J., Yu, B., Song, Z., Shang, J.: 'Analysis and design of a transverse-flux dual rotor machine for power-split hybrid electric vehicle applications', *Energies*, 2013, **6**, (12), pp. 6548–6568

[20] Wang, Y., Chau, K.T., Chan, C.C., Jiang, J.Z.: 'Transient analysis of a new outer-rotor permanent-magnet brushless dc drive using circuit-field-torque coupled time-stepping finite-element method', *IEEE Trans. Magn*., 2002, **38**, (2), pp. 1297–1300